Journal of Environmental Management 283 (2021) 111990

Contents lists available at ScienceDirect

Journal of Environmental Management

journal homepage: http://www.elsevier.com/locate/jenvman

Efficient adsorptive removal of Cobalt(II) ions from water by dicalcium phosphate dihydrate

Eleazer L. Vivas, Kuk Cho *

Department of Environmental Engineering, Pusan National University 2, Busandaehak-ro 63beon-gil, Geumjeong-gu, Busan, 46241, Republic of Korea

ARTICLE INFO

Keywords:
Adsorption
Brushite
Kinetics
Monetite
Cobalt-60

ABSTRACT

Although the radionuclide ^{60}Co is widely used, its presence in various effluents demands its removal to preclude environmental pollution and detrimental effects on human health. This study investigated the batch adsorption performance of a potential cobalt adsorbent, dicalcium phosphate dihydrate (DCPD), in immobilizing Co^{2+} from water. The influences of solution pH, contact time, initial concentration, and competing cations were examined and discussed. Stable cobalt uptake was observed at pH 4–8. The sorption kinetics showed a multi-stage uptake profile, implying that several mechanisms are involved in the adsorption process. Microscopy and structural analysis revealed that DCPD decomposes to its anhydrous form during adsorption, which explains the multistep curve over the entire adsorption period. However, the non-apatitic transformation is not exclusive to cobalt uptake. Intraparticle diffusion also contributed to the overall removal kinetics of Co^{2+} from water. Considering the Sips isotherm model, the maximum Co^{2+} adsorption capacity of DCPD was 441 mg g^{-1}. Cobalt uptake selectivity dropped in the presence of Ca^{2+} ions, from 1.21 × 10^4 to 207 mL g^{-1}, indicating DCPD would be more applicable in treating soft ^{60}Co-contaminated waters. Structural analysis, elemental mapping, and qualitative analysis of solid residues confirmed that ion exchange is involved in the removal of cobalt from aqueous solutions.

1. Introduction

Water is an essential natural resource that sustains life, livelihoods, and the environment. It plays a key role in the human body as it carries nutrients and oxygen to all body cells. However, this very role makes humans and ecosystems highly susceptible to radionuclide exposure through the unregulated or accidental release of radioactive medical, industrial, and nuclear plant wastes to bodies of water. The toxicity of radionuclides stems from their extended half-lives, high transferability and water solubility, bioavailability, and easy bioaccumulation.

Although ^{60}Co is a medium-toxicity radionuclide with a moderate half-life, it requires the same careful attention as that paid to highly toxic radionuclides such as ^{90}Sr (Dolphin et al., 1963) because its widespread field applications, close to bodies of water and residential areas, increase our vulnerability to exposure through ^{60}Co-contaminated effluents. ^{60}Co is used in radiotherapy, sterilization of medical supplies/wastes and foods, industrial radiography, density measurements, tank fill height switches, and electroplating. ^{60}Co is also found in nuclear wastewaters as a result of the neutron bombardment of stable cobalt isotopes in the metal structures of nuclear power plants. Upon exposure, skin burns, liver/kidney/bone cancers, and acute radiation sickness leading to death (EPA) can occur. Hence, its stringent reduction to permissible levels in water should be performed.

Adsorption is a promising technique for the effective removal of radionuclides from contaminated water. Adsorbents used previously in the immobilization of cobalt include unactivated attapulgite (Falayi and Ntuli, 2014), *Trichoderma reesei* (Ghaedi et al., 2013), almond green hulls (Ahmadpour et al., 2009), nano-magnesso ferrite (Srivastava et al., 2015), and apricot stone-derived activated carbon (Abbas et al., 2014). These adsorbents, however, have low cobalt uptake capacities (<115 mg g^{-1}) and should be applied at relatively higher dosage, implying more generation of post-adsorption solid residue which adds burden on secondary waste management. Calcium phosphate (CaP) minerals are potential efficient and economical ^{60}Co adsorbents. Their interactions with heavy metal ions are complex and involve several mechanisms, including ion exchange, surface dissolution-precipitation, complexation, and physisorption. Such complexity in metal uptake has gathered interest in CaPs for the effective immobilization of heavy metals (Cao

* Corresponding author.
E-mail address: kukcho@pusan.ac.kr (K. Cho).

https://doi.org/10.1016/j.jenvman.2021.111990
Received 28 October 2020; Received in revised form 16 December 2020; Accepted 11 January 2021
Available online 26 January 2021

et al., 2004; da Silva et al., 2007; Sugiyama et al., 2003).

Hydroxyapatite (HAp) (Smiciklas et al., 2006), which is a major CaP bone mineral, and swine bone char (Pan et al., 2009), which is mainly composed of HAp, carbon, and calcium carbonate, have been applied in the removal of Co^{2+} from water. However, these also exhibited low adsorption capacities (<110 mg g^{-1}) which can be attributed to the great variability in crystallinity, stoichiometry, morphology, texture, stability, and solubility of synthetic HAps (Bailliez et al., 2004; Elliott, 1994; Turner et al., 2017).

Brushite ($CaHPO_4{\cdot}2H_2O$), also known as dicalcium phosphate dihydrate (DCPD), is another CaP bone mineral which is believed to have better surface energetics and speciation than HAp for the uptake of a wide range of adsorbates (Ahmed et al., 2020). Accommodation of heavy metal ions in lattice vacancies and calcium ion substitution are known to proceed effectively in DCPD (Zhai et al., 2018). It is composed of corrugated sheets formed from zig-zag chains of bonding between CaO_8 polyhedra and PO_4^{3-} tetrahedra, and each pair of sheets is bound together through hydrogen bonds with water molecules. This feature is responsible for its lamellar layered structure (Abbona et al., 1993; Schofield et al., 2004), possibly providing more free interspaces for metal ion capture which could endow DCPD with cobalt uptake capacity higher than that of HAp. Moreover, DCPD is a known CaP cement for bone regeneration (Bohner et al., 2005; Joeris et al., 2010), implying its easy conversion into stable ceramic waste after ^{60}Co adsorption for a more manageable disposal in geological repositories. DCPD adsorbents for the uptake of Cu^{2+} (El Hamidi et al., 2014), Pb^{2+} (Ahmed et al., 2020), Sr^{2+} (Vivas et al., 2020), and Zn^{2+} (Hmimou et al., 2015) ions have been investigated, but removal mechanisms of and structural changes in the metastable adsorbent during adsorption were not addressed well. Another study focused only on the simultaneous immobilization of cadmium and arsenate through dissolution–precipitation occurring at the aqueous surface of DCPD (Zhai et al., 2018).

This study, for the first time, investigated the Co^{2+} adsorption performance of DCPD from aqueous solutions. Post-adsorption scanning electron microscopy (SEM), elemental mapping, energy dispersive X-ray spectroscopy, and powder X-ray diffractometry (PXRD) were performed to explore the removal mechanisms of and possible structural changes in DCPD upon exposure to Co^{2+} ions. The results from this study will facilitate our understanding of the potential of DCPD in the efficient removal of ^{60}Co from water. Finally, since a principal objective for the immobilization of a radioactive waste is its conversion into a leach-resistant form (IAEA, 2003; Plecas et al., 2002), adsorbent reusability was not explored.

2. Materials and methods

2.1. Reagents

Calcium chloride ($CaCl_2$, ≥95.0%) and calcium nitrate tetrahydrate ($Ca(NO_3)_2{\cdot}4H_2O$, ≥ 98.5%) were purchased from Kanto Chemical Co., Inc. (Japan). Cobalt(II) nitrate hexahydrate ($Co(NO_3)_2{\cdot}6H_2O$, ≥ 97.0%) and diammonium phosphate ($(NH_4)_2HPO_4$, ≥99%) were procured from Junsei Chemical Co., Ltd. (Japan). Hydrochloric acid (HCl, 35–37 wt%) was purchased from Samchun Pure Chemical Co., Ltd. (South Korea). Copper(II) chloride dihydrate ($CuCl_2{\cdot}6H_2O$, > 97.5%), magnesium chloride hexahydrate ($MgCl_2{\cdot}6H_2O$, > 98.0%), nitric acid (HNO_3, >69.0%), potassium chloride (KCl, > 99.0%), sodium chloride (NaCl, > 99.5%), sodium hydroxide beads (NaOH, > 98.0%), strontium chloride hexahydrate ($SrCl_2{\cdot}6H_2O$, > 98.5%), and zinc nitrate hexahydrate ($Zn(NO_3)_2{\cdot}6H_2O$, > 98.0%) were purchased from Daejung Chemicals and Metals Co., Ltd. (South Korea). Lead(II) nitrate ($Pb(NO_3)_2$, ≥99.0%) was procured from Sigma-Aldrich Chemical Company (USA). Scientific grade marine salt mix for artificial seawater (ASW) preparation was supplied by Coralife (USA). All reagents were used as received.

2.2. Preparation of DCPD powder

The adsorbent powder was prepared through a wet chemical precipitation method. Aqueous solutions of 0.40 M $Ca(NO_3)_2{\cdot}4H_2O$ in 0.68 M HCl (Solution 1, 100 mL) and 0.24 M $(NH_4)_2HPO_4$ in 0.70 M NaOH (Solution 2, 100 mL) were prepared and then refrigerated overnight at ~5 °C. Solution 2 was added at 10 mL min^{-1} to Solution 1 in a 300 mL Erlenmeyer flask placed in an ice bath with continuous stirring at 300 rpm. The resulting slurry was stirred at 500 rpm for 5 min and then refrigerated at ~5 °C for 24 h. The aged DCPD precipitates were separated from the supernatant and rinsed twice with deionized water using a Combi 514 R centrifuge (Hanil Scientific Inc., South Korea) operated at 10,000 rpm (11,057 RCF) for 10 min and then oven- and vacuum-dried for 3 h and overnight at 60 °C, respectively. The dried product was powdered using an agate mortar and pestle, screened using a Standard Test Sieve No. 200 with a 75 μm aperture (Chunggye, Seoul, South Korea), and then stored in moisture-free glass vials.

2.3. Material characterization

Images of the surface morphologies and textures of the platinum-coated raw and cobalt-substituted adsorbent powders were captured using a field emission scanning electron microscope combined with an energy dispersive X-ray spectrometer (FESEM-EDS, Ultra High Resolution Low voltage FE-SEM, JSM-7900 F Schottky, JEOL, Ltd., Japan). Elemental mapping of the powders was also conducted using FESEM-EDS. Spectral analysis was performed via Fourier transform infrared (FTIR) spectroscopy (IRAffinity-1, Shimadzu, Japan) to confirm the presence of characteristic peaks for the adsorbent before and after adsorption. The FTIR spectra were obtained from 500 to 4500 cm^{-1} at 4 cm^{-1} resolution over 120 scans. The thermal stability of the adsorbent was determined through thermogravimetric analysis in N_2 atmosphere, ramped at 5.0 °C min^{-1} (25–800 °C) at an N_2 flow rate of 20 mL min^{-1} (Simultaneous Thermal Analyzer, STA6000, PerkinElmer, United States). N_2 adsorption–desorption isotherms and surface and pore properties were acquired using a Brunauer–Emmett–Teller (BET) surface area and porosity analyzer (ASAP 2020; Micromeritics, United States) at a relative pressure range $P\,P_o^{-1} = 0.01$–1.0. The true density of the powder was determined using a 10 mL pycnometer. The structural properties of the adsorbent powders before and after adsorption were determined by powder X-ray diffraction (PXRD) using an Xpert 3 diffractometer (Malvern Panalytical Ltd., United Kingdom) with a Cu Kα radiation source. PXRD analysis was conducted at a low step scan rate (time per step = 7.14 s, scan step size = 0.026 step in 2θ/count) with a generator voltage of 40 kV and tube current of 30 mA.

Solid residues from supplemental adsorption experiments were collected and characterized. Details are provided in the supplementary data (SD p. S2).

2.4. Batch adsorption experiments

Stable Co^{2+} ions served as the surrogates for ^{60}Co. Aqueous Co^{2+} solutions of differing concentrations were prepared by dissolving $Co(NO_3)_2{\cdot}6H_2O$ in deionized water. At a solid-to-liquid (S/L) ratio of 1.0 g L^{-1}, pre-weighed DCPD powders (30 mg) were soaked in the aqueous Co^{2+} solutions (30 mL) and agitated at 185 rpm for 24 h using an orbital shaker (Daihan Scientific Co., Ltd., South Korea). All adsorption experiments were conducted at ambient temperature (T = 298 K). Elemental analysis of the liquid samples is detailed in the Analysis subsection (2.5).

The adsorption capacity (q_e) was calculated using Eq. (1), where C_o and C_e are the initial and equilibrium Co^{2+} concentrations, respectively, m is the mass of DCPD powder, and V is the volume of the aqueous Co^{2+} solution.

$$q_e = \frac{(C_o - C_e)V}{m} \quad (1)$$

The effect of pH on Co^{2+} uptake was investigated through adsorption experiments using 500 mg L^{-1} aqueous Co^{2+} solutions with different initial pH values (4–8). Drops of 0.5 M NaOH and/or 0.5 M HCl were used for pH adjustment. Subsequent adsorption experiments were conducted at neutral pH unless stated otherwise.

Using Eq. (2), the evaluation of Co^{2+} uptake kinetics was performed at C_o = 50 mg L^{-1} by determining the adsorption capacities of the samples at different contact times (q_t) before equilibrium was reached. C_t refers to the Co^{2+} concentration after a specific time t.

$$q_t = \frac{(C_o - C_t)V}{m} \tag{2}$$

Equilibrium adsorptions were carried out at different initial Co^{2+} concentrations (C_o = 25–1000 mg L^{-1}). The effect of the initial concentration on the removal efficiency (RE) was evaluated using Eq. (3).

$$RE = \left(1 - \frac{C_e}{C_o}\right)100 \tag{3}$$

The influence of competing metal ions on the selectivity of DCPD for Co^{2+} uptake in terms of distribution coefficient (K_d) in mL g^{-1}, as expressed by Eq. (4), was evaluated using equimolar (0.5 mM) aqueous Ca^{2+}, K^+, Mg^{2+}, and Na^+ solutions at neutral pH and ASW; all solutions were spiked with Co^{2+} (C_o = 25 mg L^{-1}). The raw ASW contained 332 mg L^{-1} Ca^{2+}, 368 mg L^{-1} K^+, 1.11 × 10^3 mg L^{-1} Mg^{2+}, and 9.67 × 10^3 mg L^{-1} Na^+ ions.

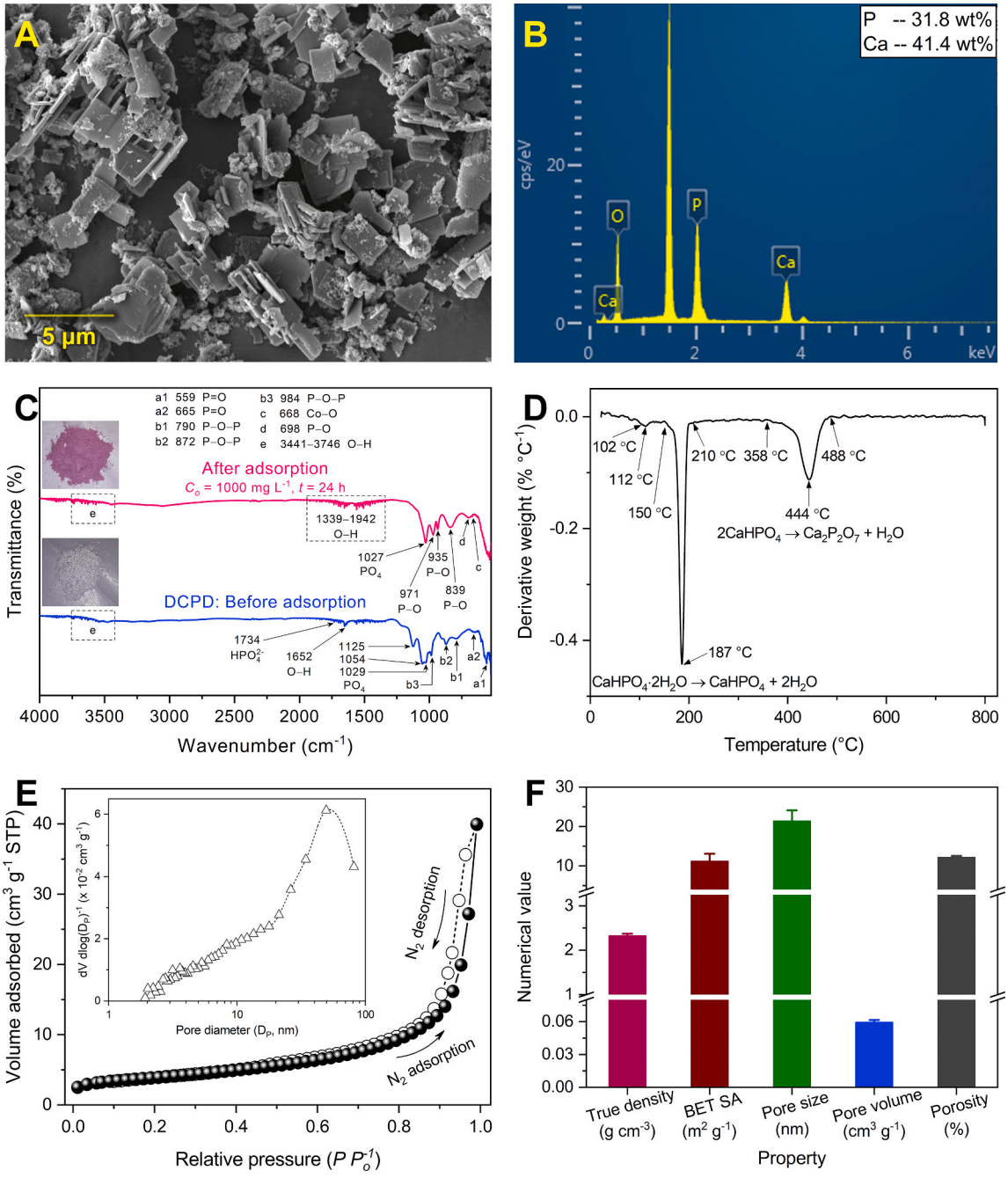

Fig. 1. Characteristics of the as-prepared DCPD powder: (A) SEM image, (B) SEM-EDS pattern (inset: elemental composition), (C) FTIR spectra before and after adsorption (inset: photos of DCPD powder and solid residue with maximum amount of immobilized cobalt), (D) thermal stability (DTG plot), (E) N_2 adsorption-desorption isotherm (inset: pore size distribution), and (F) true density, BET surface area (SA), and pore properties.

$$K_d = \left(\frac{C_o}{C_e} - 1\right)\frac{V}{m} \quad (4)$$

2.5. Analysis

Liquid samples from the adsorption experiments were transfer filtered into sample tubes using 0.2 μm cellulose acetate syringe filter units (Advantec, Toyo Roshi Kaisha, Ltd., Japan). Aliquots of the collected samples were diluted into aqueous solutions containing 3.0 wt % HNO_3 in polymethylpentene volumetric flasks. Co^{2+} concentrations were determined via flame atomic absorption spectroscopy (FAAS, AAnalyst 200, PerkinElmer, Inc., USA). Approximately 5 mL of the collected liquid samples was reserved for pH measurements using an Orion Star A211 pH meter (Orion Star A Series X21407, Thermo Scientific, Indonesia), and the remaining raw samples were stored in a cooling chamber. Qualitative analyses of the DCPD powders before and after adsorption were conducted via FESEM-EDS.

3. Results and discussion

3.1. Characteristics of DCPD powder

Since DCPD is a known precursor of HAp under physiological conditions, wet chemical precipitation synthesis was performed at low temperature under slightly acidic conditions. The SEM image (Fig. 1A) depicts stacked lath-like microsheets. The finer nanoparticles are due to sonication and grinding during sample preparation, as DCPD is known to be relatively brittle. Qualitative elemental analysis of adsorbent particles via FESEM-EDS (Fig. 1B) reveals a Ca/P ratio of ≅ 1.0. The FTIR spectrum of the as-prepared DCPD powder (Fig. 1C) shows peaks characteristic of P═O bonds at 559 and 665 cm^{-1}; at 790, 872, and 984 cm^{-1} due to P–O–P asymmetric stretching; and at 1029, 1054, and 1125 cm^{-1}, attributed to the PO_4 bond. The absorption band at 1652 cm^{-1} is due to O–H symmetric stretching, whereas the peak at 1734 cm^{-1} is ascribed to HPO_4^{2-} ions. Finally, the peaks within the 3441–3746 cm^{-1} region are for the O–H bending and stretching absorptions attributed to the structural water molecules. The derivative thermogram (Fig. 1D) indicates that DCPD is thermally stable at <150 °C and starts to decompose into anhydrous dicalcium phosphate (DCP, monetite) and calcium pyrophosphate at 151–210 °C and 358–488 °C, respectively.

The N_2 adsorption–desorption isotherms (Fig. 1E) reveal a type IV BET isotherm with an H_3-type hysteresis loop at $P\,P_o^{-1}$ ≅ 0.45, indicating that the synthesized DCPD particles have lamellar mesoporous structures, which is supported by the pore size distribution inset from the Barrett–Joyner–Halenda (BJH) model. The measured true density, BET surface area, pore size, pore volume, and porosity are 2.33 ± 0.04 g mL^{-1}, 11.22 ± 1.86 $m^2\ g^{-1}$, 21.39 ± 2.70 nm, 0.059 ± 0.002 $cm^3\ g^{-1}$, and 12.15 ± 0.38%, respectively. PXRD analysis indicates that brushite (ICDD: 98-017-2262, Fig. 2A) is the major phase of Sample D (Fig. 2D), which could be indexed using the monoclinic crystal system with the *C1c1* space group. These results, compared to those of previous reports (Frost and Palmer, 2011; Lu et al., 2020; Mourabet et al., 2011; Qin et al., 2013; Tamimi et al., 2012) and the EDS maps for Ca, Co, O, and P (Fig. 3A) confirm the successful preparation of the DCPD adsorbent powder.

3.2. Influence of pH on Co^{2+} uptake

The effect of pH on Co^{2+} removal from water was then determined. The pH range selected for this experiment was 4.0–8.0, as partial-to-complete dissolution of DCPD occurs under acidic conditions (pH < 4), and Co^{2+} ions start to precipitate as $Co(OH)_2$ at pH > 8.0, according to the speciation diagram depicted in Fig. S1.

The equilibrium Co^{2+} uptake of DCPD powder at various aqueous solution pH values is depicted in Fig. 4. The q_e values obtained across the selected pH range are similar, averaging 231.4 mg g^{-1}. Slightly acidic equilibrium pH values (~5.2) are also observed, implying a buffering effect due to the deprotonation of the ≡POH group (Mourabet et al., 2011) (Eq. (5)) and partial dissolution at the (010) face of DCPD, which liberates Ca^{2+} and HPO_4^{2-} ions (Qin et al., 2013; Zhai et al., 2018) (Eq. (6)). A pH value of 7.0 was selected for subsequent adsorption experiments, as it is more practical and within the US EPA permissible pH range (6.0–9.0) for effluents.

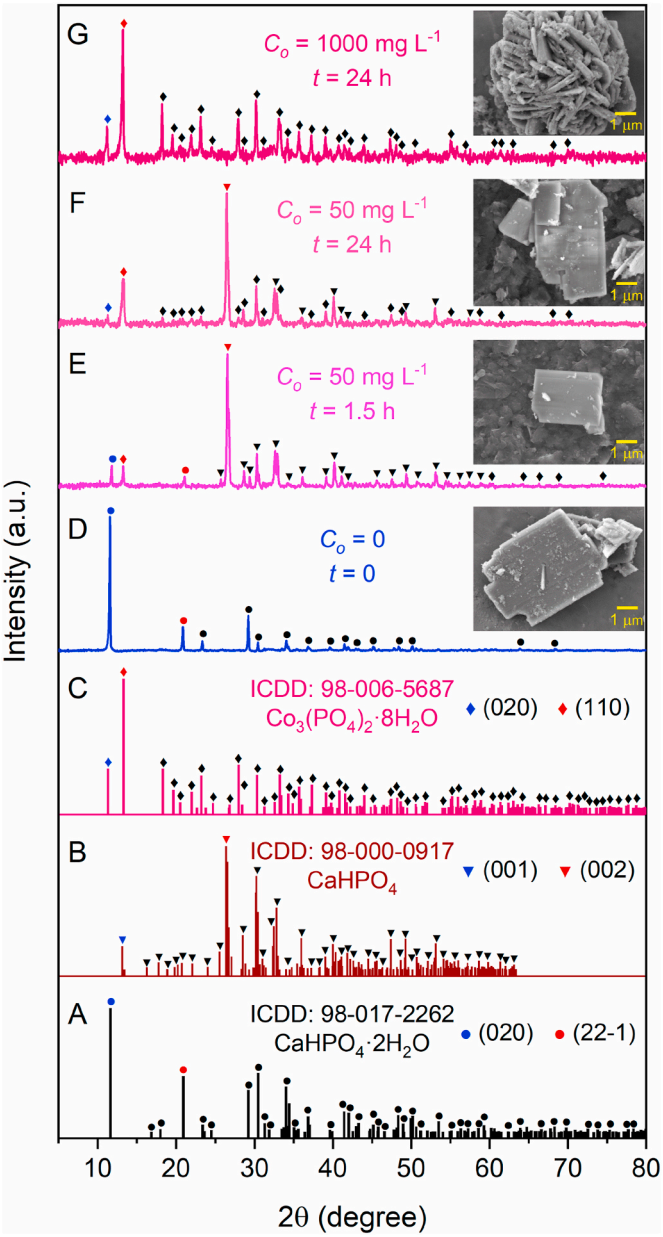

Fig. 2. PXRD patterns: Reference diffractograms of (A) monoclinic brushite, (B) anorthic monetite, and (C) monoclinic $Co_3(PO_4)_2{\cdot}8H_2O$; (D–G) diffractograms of the samples with SEM images of adsorbent before and after adsorption.

$$\equiv P - OH_{(s)} + \ H_2O_{(l)} \rightleftharpoons \equiv P - O^-_{(s)} + H_3O^+_{(aq)} \quad (5)$$

$$HPO^{2-}_{4(aq)} + H_2O_{(l)} \rightleftharpoons PO^{3-}_{4(aq)} + H_3O^+_{(aq)} \quad (6)$$

The high q_e values are most likely due to Ca^{2+}–Co^{2+} ion exchange and complexation of the Co^{2+} ions by the $\equiv PO^-$ groups in DCPD, which are deprotonated at pH ≅ 7.0 (the point of zero charge of DCPD is pH ~5.5) (Daskalakis and Nancollas, 1994). Simultaneous partial

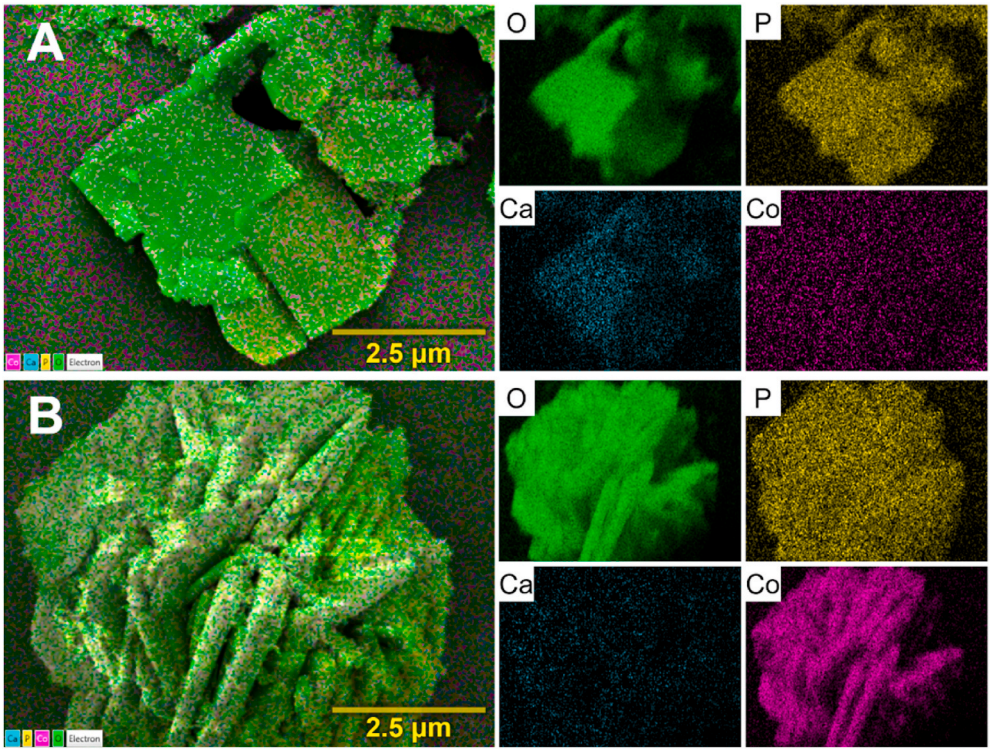

Fig. 3. SEM-EDS maps of (A) raw DCPD and (B) collected solid residue after 24-h adsorption at C_o = 1000 mg L^{-1}. General adsorption conditions: S/L = 1.0 g L^{-1}, pH = 7.0, 185 rpm, T = 25 °C.

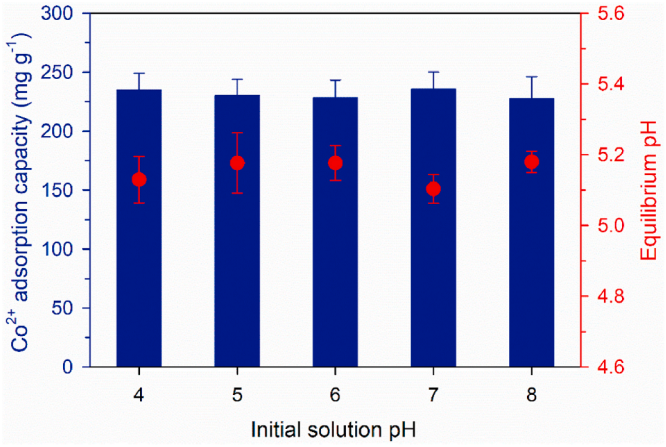

Fig. 4. pH effect on Co^{2+} uptake at C_o = 500 mg L^{-1}. General adsorption conditions: S/L = 1.0 g L^{-1}, 185 rpm, T = 25 °C.

dissolution–epitaxial deposition of hydrated cobalt phosphate is also likely to occur, according to related literature (Qin et al., 2013; Zhai et al., 2018).

3.3. Co^{2+} uptake kinetics

The classical pseudo-first-order (PFO) and pseudo-second-order (PSO) reaction kinetics models (Ho, 1998; Langergren, 1898), expressed by Eqs. (7) and (8), respectively, were tested to determine the kinetics behavior of Co^{2+} uptake by DCPD. Nonlinear regression was applied, as it is more reliable than linear regression (Xiao et al., 2018). The intraparticle diffusion (IPD) model expressed by Eq. (9) (Weber and Morris, 1963) was also considered to determine if IPD has any contribution to Co^{2+} uptake by DCPD. The goodness of fit of the nonlinear regressions were evaluated using correlation coefficient (r^2) and standard error of estimate (SE) values which were calculated through the SigmaPlot® 10.0 software.

$$q_t = q_e\left(1 - e^{-k_1 t}\right) \tag{7}$$

$$q_t = \frac{k_2 q_e^2 t}{1 + k_2 q_e t} \tag{8}$$

$$q_t = k_{ip} t^{0.5} \tag{9}$$

Here, k_1 (min^{-1}), k_2 (g mg^{-1} min^{-1}), and k_{ip} (mg g^{-1} $min^{-0.5}$) are the PFO, PSO, and IPD rate constants, respectively.

The kinetics results from the adsorption experiments are depicted in Fig. 5 and summarized in Table 1. The inset in Fig. 5A reveals that Co^{2+} adsorption by DCPD is slow, requiring 4 and 24 h to remove 43.8% and 91.7% of the Co^{2+} ions from water, respectively. This observation is supported by the low rate constant values for both kinetics models (Table 1). Nevertheless, the Co^{2+} adsorption better fitted the PSO model (Fig. 5A), as corroborated by its higher r^2 and lower SE (Table 1). However, a large difference between the experimental and calculated q_e values is observed, implying possible multistage cobalt uptake kinetics with two equilibrium stages having different reaction orders. Thus, the data points were replotted as depicted in Fig. 5B, which shows a multistage uptake kinetics profile that largely deviates from the single-stage kinetics data. An initial plateau is observed after 1 h; then, q_t starts to rise again until reaching a second plateau after 24 h. From the r^2 and SE values and comparison of calculated and experimental q_e values (Table 1), the first and second equilibrium stages best fitted the PSO and PFO models, respectively.

Since various removal mechanisms can occur simultaneously on DCPD, SEM imaging and structural analysis of the solid residues from the adsorption experiments were conducted to better elucidate the unusual Co^{2+} uptake kinetics profile. Sample E (Fig. 2E), which is representative of the inflection region of the curve, appears to retain a lath-

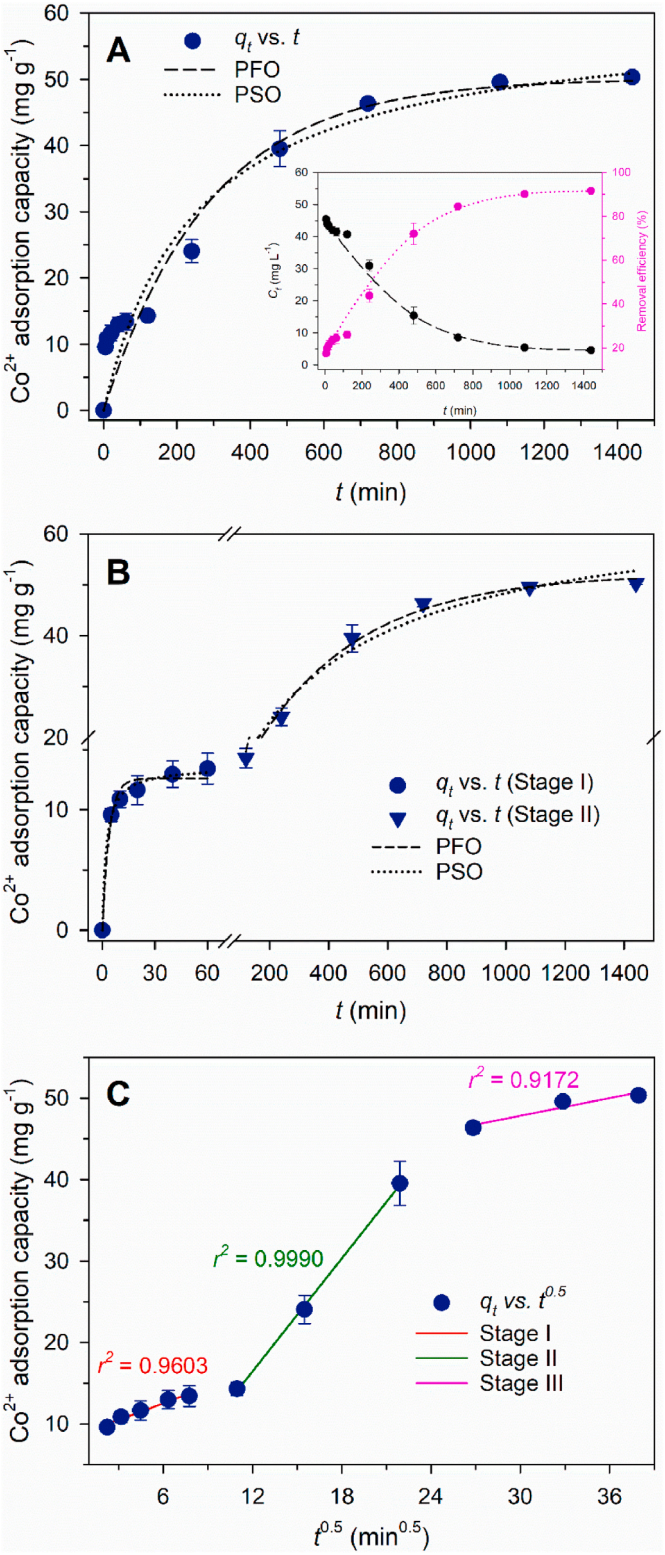

Fig. 5. Co^{2+} uptake kinetics at C_o = 50 mg L^{-1} using DCPD adsorbent powder (q_t vs. t): (A) single (inset: C_t vs. t, *RE* vs. t) and (B) multiple nonlinear regressions of PFO and PSO reaction kinetics models and (C) multilinear plots for IPD model. General adsorption conditions: S/L = 1.0 g L^{-1}, pH = 7.0, 185 rpm, T = 25 °C.

Table 1
Adsorption kinetics constants of Co^{2+} on DCPD.

Stage	Model parameters	Values
–	**PFO**	
	q_e (mg g^{-1}), exp	50.3
	q_e (mg g^{-1}), calc	50.1
	k_1 (min^{-1})	3.46 × 10^{-3}
	r^2	0.9108
	SE	5.6051
	PSO	
	q_e (mg g^{-1}), exp	50.3
	q_e (mg g^{-1}), calc	59.8
	k_1 (min^{-1})	6.63 × 10^{-5}
	r^2	0.9204
	SE	5.2953
I	**PFO**	
	q_e (mg g^{-1}), exp	13.4
	q_e (mg g^{-1}), calc	12.6
	k_1 (min^{-1})	2.56 × 10^{-1}
	r^2	0.9809
	SE	0.7689
	PSO	
	q_e (mg g^{-1}), exp	13.4
	q_e (mg g^{-1}), calc	13.6
	k_1 (min^{-1})	3.21 × 10^{-2}
	r^2	0.9958
	SE	0.3592
II	**PFO**	
	q_e (mg g^{-1}), exp	50.3
	q_e (mg g^{-1}), calc	52.2
	k_1 (min^{-1})	2.79 × 10^{-3}
	r^2	0.9950
	SE	1.1845
	PSO	
	q_e (mg g^{-1}), exp	50.3
	q_e (mg g^{-1}), calc	66.6
	k_1 (min^{-1})	3.98 × 10^{-5}
	r^2	0.9778
	SE	2.4843

like morphology. However, its PXRD pattern implies that DCPD is transformed into its anhydrous form (dicalcium phosphate or monetite, DCP) because of the observed significant decline in the intensity of the monoclinic brushite phase and higher intensity of the anorthic monetite phase (ICDD: 98-000-0917). The presence of a low-intensity monoclinic cobalt phosphate octahydrate ($Co_3(PO_4)_2{\cdot}8H_2O$, CPO) phase (ICDD: 98-006-5687) is also detected, confirming Co^{2+} immobilization. Sample F (Fig. 2F) has a morphology similar to those of Samples D (Fig. 2D) and E (Fig. 2E), but its PXRD pattern reveals the complete disappearance of brushite and the retention of monetite (high intensity) and CPO (higher intensity) phases. From these results, the end of the plateau for the first equilibrium stage (t = 1.0 h) indicates a kinetic balance between the saturation of the DCPD surface adsorption sites with Co^{2+} ions and the decomposition of DCPD to DCP, while the end of the second plateau (t = 24 h) signifies a kinetic balance among the Co^{2+} removal mechanisms for the saturation of DCP. However, the mechanism by which DCPD was kinetically transformed into DCP in the presence of Co^{2+} ions and the exclusivity of this phenomenon to this adsorbate required elucidation. Hence, further structural analysis was conducted.

According to previous studies, DCPD is transformed to DCP after 45 min under hydrothermal treatment (Mohd Shafie et al., 2017) in alkaline solution after 35 min at 60 °C (Rocha et al., 2018) and in deionized water at 70 °C for 1 d (Tas and McKittrick, 2016). The PXRD patterns depicted in Fig. S2C–D reveal that soaking DCPD in pure deionized water or neutral water at 25 °C alone transforms it to DCP. This can be attributed to progressive dissolution at the DCPD (010) cleavage surfaces, mainly proceeding by the formation and spreading of etch pits, as highlighted in previous studies (Qin et al., 2013; Tang et al., 2003; Zhai et al., 2018). Dissolution at the DCPD–water interface releases Ca^{2+} and HPO_4^{2-}, the former having two molecules of coordinated water (Schofield et al., 2004) that are constituents of the structural water bilayers

parallel to the (020) face of the DCPD crystal (Arsic et al., 2004). Finally, the hydrogen bonds between water and HPO_4^{2-} are broken when the crystal discontinuity interrupts the bilayers of water molecules (Tas and McKittrick, 2016). PXRD patterns of the solid residues after 24-h agitated soaking of the DCPD powder in 0.85 mM aqueous solutions of Co^{2+} (equivalent to 50 mg L^{-1}), Cu^{2+}, Pb^{2+}, Sr^{2+}, and Zn^{2+} (Fig. S2E–I) reveal that DCPD decomposes to DCP, given that the intensities of the characteristic (020) and (22–1) Bragg peaks for the brushite phase vanish and the characteristic high intensity (002) and (001) Bragg peaks of the anorthic monetite phase appear. This is also corroborated by the less-compacted plate-like particles depicted in Fig. S3A–C, as compared to the pristine DCPD (Fig. 1A). These results imply that the structural decomposition of DCPD is not exclusive to Co^{2+} exposure. In aqueous solutions of divalent or multivalent metal cations, the transformation of DCPD still occurs owing to dissolution but becomes coupled with epitaxial precipitation. Zhai et al. (2018) directly observed the dissolution–precipitation processes at the DCPD–water interface using cadmium- and arsenic-containing aqueous solutions. They showed the dissolution of DCPD crystals and the subsequent precipitation of cadmium and arsenic phosphates on the DCPD surface after certain induction periods.

Fig. 5C shows multilinear plots of q_t versus $t^{0.5}$, which suggest that three stages of mass diffusion are involved in the overall removal of Co^{2+} from water. The initial slow uptake (Stage I) can be attributed to boundary diffusion, which contributes to the saturation of the surface adsorption sites of DCPD in the first equilibrium stage of the reaction uptake kinetics profile (Fig. 5B). Thereafter, rapid IPD occurs to saturate the interior of the decomposed DCPD particles. The last plot may pertain to slow IPD, as the diffusion barrier at the surface of the adsorbent thickens owing to the adsorbed Co^{2+} ions and layer of precipitated CPO. The rapid and slow IPD (Stages II and III, Fig. 5C) processes may contribute to the rapid and slow adsorption steps in the second equilibrium stage of the uptake kinetics profile (Fig. 5B), respectively. The rapid IPD stage seems to be the rate determining step at t = 120–480 min, as it has the highest r^2. The calculated k_{ip} over this time period is 2.31 mg g^{-1} $min^{-0.5}$. However, IPD is not the rate-controlling step for Co^{2+} uptake over the entire sorption period since the plot does not pass through the origin.

3.4. Equilibrium adsorption isotherms

The Co^{2+} *REs* by DCPD were evaluated at various C_o values. The uptake capacity rises with increasing C_o until equilibrium is reached. The highest average *RE* (~92.5%) is achieved at C_o = 25.0 and 50.0 mg L^{-1} (Fig. 6A inset), demonstrating the potential applicability of the adsorbent in treating low-level ^{60}Co-contaminated waters. The Co^{2+} adsorption capability of DCPD was evaluated by fitting the C_e values into the Langmuir (Eq. (10)), Freundlich (Eq. (11)), and Sips (Eq. (12)) adsorption isotherm models. The nonlinear fitting of the equilibrium adsorption results was preferred, as mathematical linearization of the nonlinear model equations resulted in biased estimates of the isotherm constants, which may lead to misinterpretations (Tsai and Juang, 2000). The goodness of fit of the nonlinear isotherms to the experimental equilibrium data was also assessed using computed r^2 and *SE* values.

$$q_e = \frac{q_m K_L C_e}{1 + K_L C_e} \tag{10}$$

$$q_e = K_F C_e^{\frac{1}{n_F}} \tag{11}$$

$$q_e = \frac{q_S K_S C_e^{n_S}}{1 + K_S C_e^{n_S}} \tag{12}$$

Here, q_m (mg g^{-1}) and q_S (mg g^{-1}) pertain to the Langmuir and Sips maximum uptake capacities, respectively; K_L (L mg^{-1}) is the Langmuir constant referring to the rate of adsorption; K_F (mg g^{-1} (L $mg^{-1})^{1/n}$) is the Freundlich constant which is associated with multilayer adsorption capacity; K_S ((L $mg^{-1})^n$) is the Sips constant which denotes adsorption energy; and n_F and n_S are the dimensionless parameters representing Freundlich adsorption intensity and Sips system heterogeneity,

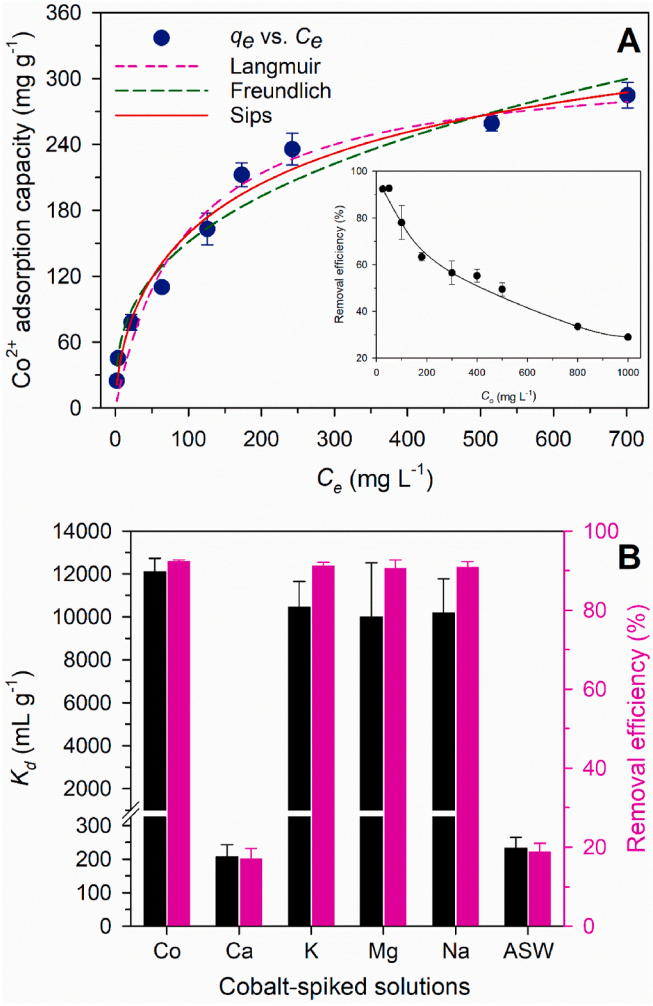

Fig. 6. Equilibrium Co^{2+} adsorption performance and selectivity of DCPD powder: (A) q_e vs. C_e at varied C_o = 25–1000 mg L^{-1} with fittings of Langmuir, Freundlich, and Sips models (inset: *RE* at various C_o); (B) selectivity results (K_d values and *RE*) using 25 mg L^{-1} aqueous Co^{2+} solution and cobalt-spiked (C_o = 25 mg L^{-1}) 0.5 mM Ca^{2+}/K^+/Mg^{2+}/Na^+ aqueous solutions, and ASW. General adsorption conditions: S/L = 1.0 g L^{-1}, pH = 7.0, 185 rpm, T = 25 °C.

Table 2
Adsorption isotherm constants for Co^{2+} on DCPD powders.

Model and parameters	Values
Langmuir	
q_m (mg g^{-1})	317
K_L (L mg^{-1})	1.03×10^{-2}
r^2	0.9648
SE	19.3649
Freundlich	
K_F (mg g^{-1} (L $mg^{-1})^{1/n}$)	30.0
n_F	2.85
r^2	0.9637
SE	19.6499
Sips	
q_S (mg g^{-1})	441
K_S (L $mg^{-1})^n$	3.29×10^{-2}
n_S	0.62
r^2	0.9778
SE	16.2259

respectively. Fig. 6A shows the nonlinear adsorption isotherms and Table 2 summarizes the calculated isotherm constants and q_e values.

Compared to the previously studied synthetic HAp (Smiciklas et al., 2006) and swine bone char (Pan et al., 2009), whose Co^{2+} sorption isotherms follow either Langmuir or Dubinin–Kaganer–Radushkevich and Freundlich models, respectively, the Co^{2+} adsorption isotherm for DCPD best fits the Sips model ($r^2 = 0.9788$, $SE = 16.2259$, Table 2), which implies that Co^{2+} uptake is a heterogeneous process and not limited to monolayer ion exchange. The calculated n_S of ~0.62 ($n_S \leq 1$) suggests that the interactions of the Co^{2+} ions with the adsorption sites closely resemble the function of the Langmuir–Freundlich model. The calculated maximum Sips Co^{2+} uptake capacity ($q_S = 441$ mg g^{-1}) of DCPD is significantly higher than that of HAp and one of the highest among those of the previously investigated non-CaP adsorbents summarized in Table 3.

Although cobalt uptake seems to plateau after 24 h at $C_o = 1000$ mg L^{-1}, qualitative analysis (Fig. S4D) shows that remnant calcium is not replaced by cobalt. The calculated q_S is lower than the theoretical maximum Co^{2+} adsorption capacity of ~514 mg g^{-1}, according to the stoichiometry of the reactions in Eqs. (13) and (14).

The solid residue recovered after soaking DCPD in 1000 mg L^{-1} Co^{2+} solution, which has the maximum amount of immobilized cobalt, was characterized. The FTIR spectrum (Fig. 1C) shows characteristic peaks that match those of synthetic CPO (Li et al., 2015). Qualitative confirmation of the successful immobilization of Co^{2+} ions is observed through optical comparison and SEM-EDS elemental mapping. The insets in Fig. 1C show an evident color change from the white DCPD powder to a pink solid residue that resembles CPO. The EDS maps depicted in Fig. 3B reveal a cobalt-rich solid residue. The PXRD pattern of Sample G (Fig. 2G) is an identical match to that of CPO, which can be indexed in the monoclinic crystal system (ICDD: 98-006-5687) with the *C12/m1* space group. It should be noted that comparing only the PXRD patterns of pristine DCPD and Sample G would give a misleading deduction that DCPD does not undergo any structural change during Co^{2+} adsorption, as DCPD and CPO are both monoclinic crystals. Thus, it is false to conclude that "topotactic" ion-exchange is involved in cobalt immobilization using DCPD. The inset in Fig. 2G reveals an agglomerated particle of Sample G with flower-like morphology; this structure is clearer in the low-magnification SEM image depicted in Fig. S3D. Previous studies revealed that hydrated cobalt phosphate microsheets interconnect into self-assembled 3D flower-like particles in aqueous solutions (Bach et al., 2016; Li et al., 2015, 2018), most probably owing to hydrogen bonds of the water molecules coordinated to immobilized Co^{2+} ions.

3.5. Selectivity evaluation: Effect of competitive cations on K_d

Co^{2+} uptake by DCPD was evaluated using cobalt-spiked aqueous solutions and ASW, and the calculated K_d values are presented in Fig. 6B and Table 3. DCPD demonstrates the K_d of 1.21×10^4 mL g^{-1}, which is comparable to previous reports, in the absence of naturally prevalent cations in water ($C_o = 25$ mg L^{-1}). The K_d and RE values drastically decline in aqueous Co^{2+}/Ca^{2+} solution ($K_d = 206.6 \pm 36.5$ mL g^{-1}, $RE = 17.1 \pm 2.6\%$) and ASW ($K_d = 232.9 \pm 31.6$ mL g^{-1}, $RE = 18.9 \pm 2.1\%$). K^+, Na^+, and Mg^{2+} ions cause slight reductions (considering the error bars) in the K_d and RE values. The discussion of the influence of competitive cations on Co^{2+} uptake selectivity can be divided into three parts:

- Ca^{2+} is a parent cation in DCPD; therefore, its resorption is more preferable than the uptake of Co^{2+} and monovalent cations such as K^+ and Na^+. Ca^{2+} is expected to compete strongly with Co^{2+} for the adsorption sites through ion exchange.
- Even though Mg^{2+} is a divalent cation like Ca^{2+}, it has a smaller ionic radius (0.65 Å) than Ca^{2+} (0.99 Å) and Co^{2+} (0.72 Å) (Nightingale, 1959); however, it prefers to exist in its hydrated form in aqueous solutions. Hydrated Mg^{2+} has two layers of hydration shells, making the radius of its hydrated form 400 times larger than that of its dehydrated form (Jahnen-Dechent and Ketteler, 2012). Thus, it has a high dehydration energy requirement which hinders its entry into the sorption sites of the adsorbent. Additionally, Mg^{2+} is the hardest Lewis acid among the cations investigated (i.e., $Mg^{2+} > Na^+ > Ca^{2+} > K^+ > Co^{2+}$) (Pearson, 1988) according to the hard and soft acids and bases concept, possibly causing it to have weaker affinity to phosphate anions.
- The reduction in K_d by ASW should be larger than that by aqueous Ca^{2+} solution since ASW has a greater amount of DCPD-selective Ca^{2+} ions. However, the ionic strength (IS) of aqueous solutions, which affects the stability of colloids in terms of double layer and hydration interactions, is an important consideration. The significantly higher IS of ASW (~0.61 M) than that of aqueous Ca^{2+} solution (2.77×10^{-3} M) probably causes a thinning of the electrical double layer and a decrease in the attractive electrostatic force between the adsorption sites and cations, thereby constraining the diffusion of both Ca^{2+} and Co^{2+} ions into the adsorbent. In terms of hydration, the high concentration of electrolyte ions in ASW could stabilize the hydrated forms of Co^{2+} and Ca^{2+} (Manciu and Ruckenstein, 2001; Ruiz-Agudo et al., 2011), hampering the epitaxial precipitation of CPO and resorption of parent Ca^{2+} ions. Furthermore, the high IS could gradually intensify the ion–ion interactions between Co^{2+} and NO_3^- and Ca^{2+} and Cl^-, increasing the volume of the hydration shell (Marx et al., 2010); therefore, the K_d value is not decreased more in ASW than in Ca^{2+} solution.

Since DCPD demonstrates low Co^{2+} selectivity in the presence of

Table 3
Comparative summary of q_m and K_d values of previously investigated Co^{2+} adsorbents.

Adsorbent Type	Name	S/L	q_m, mg g^{-1}	Adsorption conditions for K_d				Ref.
				Co^{2+} solution	C_o, mg L^{-1}	pH	K_d, mL g^{-1}	
CaP	*DCPD*	1.0	*441*	Aqueous	25	7.0	*1.21×10^4*	*This study*
			–	Spiked ASW	25	7.6	*2.33×10^2*	*This study*
	HAp	5.0×10^{-3}	20.9	–	–	–	–	Smiciklas et al. (2006)
	Swine bone char	10	109	–	–	–	–	Pan et al. (2009)
Clay mineral	Unactivated attapulgite	100	4.00×10^{-4}	Mine drainage	19.8	2.8	194[a]	Falayi and Ntuli (2014)
Biosorbent	*Trichoderma reesei*	4.0	80.6	Aqueous	30	5.0	1.23×10^4[a]	Ghaedi et al. (2013)
	Saccharum bengalense pulp	10	14.5	Aqueous	50	6.0	150[a]	Imran Din et al. (2013)
Agri-waste	Almond Green hull	5.0	45.5	Aqueous	17.8	–	1.31×10^4[a]	Ahmadpour et al. (2009)
Composite	n-$MgFe_2O_4$	6.0	67.4	Aqueous	200	–	7.08×10^3[a]	Srivastava et al. (2015)
	PGBS-COOH	2.0	167	Aqueous	25	6.5	4.96×10^4[a]	Shibi and Anirudhan (2005)
	(MB-IA)-g-MNCC	2.0	350	–	–	–	–	Anirudhan et al. (2018)
Carbon-based	Apricot stone activated carbon	5.0	111	–	–	–	–	Abbas et al. (2014)
	Ozonized graphene oxides	0.1	372	Aqueous	20	6.8	7.42×10^3[a]	Liu et al. (2016)

[a] Calculated from the available adsorption data of the reference.

Ca^{2+}, its potential field application could be explored for the treatment of soft ^{60}Co-contaminated waters. Prospective practical configurations include solid-supported DCPD composite packing adsorbent materials and membrane adsorbent filters in packed bed columns and filtration cartridges, respectively.

3.6. Removal mechanisms

The PXRD patterns (Fig. 2), elemental maps (Fig. 3), and SEM-EDS qualitative analysis (Fig. S4) showed that ion exchange (Eq. (13)) is involved in cobalt removal from aqueous solutions. Similar to that reported in our previous work on strontium adsorption using brushite-infused polyacrylonitrile nanofibers (Vivas et al., 2020), complexation with $\equiv PO^-$ groups (Eq. (14)) probably contributes to Co^{2+} ion immobilization.

The cobalt uptake kinetics by DCPD is quite slow compared to other Co^{2+} adsorbents. Valsami-Jones et al. (1998) also observed a low adsorption rate in the sequestration of Pb^{2+} using bone char, whereas Zhai et al. (2018) examined the deposition of hydrated cadmium and arsenic phosphates on DCPD surfaces. Combining their findings and comparing those to ours, the slow cobalt uptake over the entire sorption period can be attributed to the epitaxial deposition of CPO (Eq. (6) and (15)) on the adsorbent (*vide infra*). The rapid and slow cobalt uptake steps of the first equilibrium stage (Fig. 5B) can be attributed to saturation of the surface adsorption sites of DCPD through ion exchange, complexation, and coupled dissolution–epitaxial precipitation of CPO, which are assisted by slow boundary diffusion (Stage I, Fig. 5C). After the crystal transformation from DCPD to DCP, the IPD of cobalt into the crystal accelerates (Stage II, Fig. 5C), along with the acceleration of adsorption reaction kinetics, because new adsorption sites become available. Cobalt uptake reactions continue, albeit at a lower rate, during the second equilibrium stage (Stage II, Fig. 5B) due to the deposited CPO layer, which probably becomes an effective barrier. As the CPO layer thickens, the diffusion barrier resistance increases. This decelerates both the IPD of Co^{2+} into the adsorbent to exchange or form complexes with Ca^{2+} or $\equiv PO^-$, respectively, and the dissolution–precipitation process as depicted harmoniously by the second plateau of Fig. 5B and slow IPD (Stage III) of Fig. 5C. This complex cobalt uptake kinetics might be the reason for the disparity between the computed q_S and theoretical maximum uptake capacity. Nevertheless, the CPO layer becomes an effective diffusion barrier (Pan et al., 2009), embedding the initially sorbed Co^{2+} ions into the adsorbent structure, which suggests the possibility of high-to-permanent retention of the adsorbed cobalt within the solid residue (Zhai et al., 2018). This is advantageous in the conversion of the cobalt-saturated CaP residues into ceramic wastes for more manageable disposal in geological repositories.

$$CaHPO_4{\cdot}2H_2O_{(s)} + xCo^{2+}_{(aq)} + yH_2O_{(l)} \rightarrow Ca_{1-x}Co_xHPO_4{\cdot}(2+y)H_2O_{(s)} + xCa^{2+}_{(aq)} \quad (13)$$

$$2(DCPD - O^-)_{(s)} + Co^{2+}_{(aq)} + yH_2O_{(aq)} \rightarrow (DCPD - O)_2Co{\cdot}yH_2O_{(s)} \quad (14)$$

$$3Co^{2+}_{(aq)} + 2PO^{3-}_{4\ (aq)} + 8H_2O_{(l)} \rightarrow Co_3(PO_4)_2{\cdot}8H_2O_{(s)} \quad (15)$$

4. Conclusions

DCPD, which was expected to have a higher adsorption capacity than conventional HAp, was used to remove Co^{2+} from water for the first time. Single nonlinear fitting of the cobalt adsorption kinetics data over the entire time range conformed with the PSO model, but multi-nonlinear regression analysis showed an unusual uptake kinetics behavior. SEM imaging and structural analysis of the solid residues revealed that DCPD decomposes to DCP during Co^{2+} adsorption. However, supplemental investigation indicated that the non-apatitic transformation of DCPD was not exclusive to cobalt. The findings of the adsorption experiments, backed by structural and qualitative analyses of solid residues, indicated that at least three mechanisms (i.e., ion exchange, partial dissolution–precipitation, and complexation) were involved in the adsorption process and were likely to occur simultaneously. IPD also contributed to the overall kinetics of Co^{2+} removal from water. The Sips model best described the sorption data, according to the equilibrium adsorption isotherm studies. Although the cobalt uptake rate and selectivity in the presence of several competing cations were low, DCPD still effectively adsorbed cobalt from aqueous solutions ($q_S = 441$ mg g^{-1}). DCPD exhibited consistent cobalt uptake in the pH range of 4–8. The results of this study confirm the potential application of DCPD as a ^{60}Co adsorbent that could satisfy the objectives of radioactive waste management. A future research consideration is the exploration of solid-supported DCPD adsorbents as packed bed column materials or composite membrane filters for the adsorptive filtration of effluents for a more manageable ^{60}Co removal process.

Credit author statement

Eleazer L. Vivas: Conceptualization, Methodology, Investigation, Writing – original draft; Kuk Cho: Validation, Writing – review & editing.

Funding

This work was supported by the National Research Foundation (NRF) grant, which is funded by the Ministry of Science and ICT, Republic of Korea (2019R1A2C1084995), and by the Basic Science Research Program through the NRF, which is funded by the Ministry of Education, Republic of Korea (2020R1A6A1A03044834).

Declaration of competing interest

The authors declare that they have no known competing financial interests or personal relationships that could have appeared to influence the work reported in this paper.

Acknowledgment

The authors thank Editage (www.editage.co.kr) for English language editing of the manuscript.

Appendix A. Supplementary data

Supplementary data to this article can be found online at https://doi.org/10.1016/j.jenvman.2021.111990.

References

Abbas, M., Kaddour, S., Trari, M., 2014. Kinetic and equilibrium studies of cobalt adsorption on apricot stone activated carbon. J. Ind. Eng. Chem. 20, 745–751.
Abbona, F., Christensson, F., Franchini Angela, M., Lundager Madsen, H.E., 1993. Crystal habit and growth conditions of brushite, $CaHPO_4{\cdot}2H_2O$. J. Cryst. Growth 131, 331–346.
Ahmadpour, A., Tahmasbi, M., Bastami, T.R., Besharati, J.A., 2009. Rapid removal of cobalt ion from aqueous solutions by almond green hull. J. Hazard Mater. 166, 925–930.
Ahmed, M.K., Mansour, S.F., Ramadan, R., Afifi, M., Mostafa, M.S., El-dek, S.I., Uskoković, V., 2020. Tuning the composition of new brushite/vivianite mixed systems for superior heavy metal removal efficiency from contaminated waters. Journal of Water Process Engineering 34.
Anirudhan, T.S., Shainy, F., Deepa, J.R., 2018. Effective removal of Cobalt(II) ions from aqueous solutions and nuclear industry wastewater using sulfhydryl and carboxyl functionalised magnetite nanocellulose composite: batch adsorption studies. Chem. Ecol. 35, 235–255.
Arsic, J., Kaminski, D., Poodt, P., Vlieg, E., 2004. Liquid ordering at the Brushite-{010}–water interface. Phys. Rev. B 69.
Bach, S., Panthöfer, M., Bienert, R., Buzanich, A.d.O.G., Emmerling, F., Tremel, W., 2016. Role of water during crystallization of amorphous cobalt phosphate nanoparticles. Cryst. Growth Des. 16, 4232–4239.

Bailliez, S., Nzihou, A., Bèche, E., Flamant, G., 2004. Removal of lead (Pb) by hydroxyapatite sorbent. Process Saf. Environ. Protect. 82, 175–180.
Bohner, M., Gbureck, U., Barralet, J.E., 2005. Technological issues for the development of more efficient calcium phosphate bone cements: a critical assessment. Biomaterials 26, 6423–6429.
Cao, X., Ma, L.Q., Rhue, D.R., Appel, C.S., 2004. Mechanisms of lead, copper, and zinc retention by phosphate rock. Environ. Pollut. 131, 435–444.
da Silva, O.G., da Fonseca, M.G., Arakaki, L.N.H., 2007. Silylated calcium phosphates and their new behavior for copper retention from aqueous solution. Colloid. Surface. Physicochem. Eng. Aspect. 301, 376–381.
Daskalakis, K.D., Nancollas, G.H., 1994. Dicalcium phosphate dihydrate crystal growth in the pH region of 4.5 to 6.2. In: Amjad, Z. (Ed.), American Chemical Society Symposium on Mineral Scale Formation and Inhibition. Springer Science+Business Media, Washington, D.C., USA, pp. 219–230.
Dolphin, G.W., Fairbairin, A., Jammet, H., Rogers, L.R., 1963. A Basic Toxicity Classification of Radionuclides, Technical Reports Series. International Atomic Energy Agency, IAEA, Kamtner Ring 11, Vienna I, Austria, p. 33.
El Hamidi, A., Mulongo Masamba, R., Khachani, M., Halim, M., Arsalane, S., 2014. Kinetics modeling in liquid phase sorption of copper ions on brushite di-calcium phosphate di-hydrate $CaHPO_4{\cdot}2H_2O$ (DCPD). Desalination and Water Treatment 56, 779–791.
Elliott, J.C., 1994. Structure and Chemistry of the Apatites and Other Calcium Orthophosphates. Elsevier Science B.V., Sara Burgerhartstraat 25, P.O. Box 211, 1000 AE Amsterdam, The Netherlands.
EPA, EPA Facts about Cobalt-60. United States Environmental Protection Agency.
Falayi, T., Ntuli, F., 2014. Removal of heavy metals and neutralisation of acid mine drainage with un-activated attapulgite. J. Ind. Eng. Chem. 20, 1285–1292.
Frost, R.L., Palmer, S.J., 2011. Thermal stability of the 'cave' mineral brushite $CaHPO_4{\cdot}2H_2O$ – mechanism of formation and decomposition. Thermochim. Acta 521, 14–17.
Ghaedi, M., Hajati, S., Karimi, F., Barazesh, B., Ghezelbash, G., 2013. Equilibrium, kinetic and isotherm of some metal ion biosorption. J. Ind. Eng. Chem. 19, 987–992.
Hmimou, J.E.S., Rifi, E.H., Lebkiri, A., Ebn Touhami, M., Hatim, Z., 2015. Equilibrium and kinetic modeling of Zn(II) adsorption from aqueous solution using dicalcique dehydrated. Moroccan Journal of Chemisty 3, 263–271.
Ho, Y.S., McKay, G., 1998. Sorption of dye from aqueous solution by peat. Chem. Eng. J. 70, 115–124.
IAEA, 2003. Radioactive waste management glossary, 2003. In: International Atomic Energy Agency, International Atomic Energy Agency, Wagramer Strasse 5, P.O. Box 100, A-1400 Vienna, Austria.
Imran Din, M., Mirza, M.L., Ata, S., Athar, M., Mohsin, I.U., 2013. Thermodynamics of biosorption for removal of Co(II) ions by an efficient and ecofriendly biosorbent (saccharum bengalense): kinetics and isotherm modeling. J. Chem. 2013, 1–11.
Jahnen-Dechent, W., Ketteler, M., 2012. Magnesium basics. Clin Kidney J 5, i3–i14.
Joeris, A., Ondrus, S., Planka, L., Gal, P., Slongo, T., 2010. ChronOS inject in children with benign bone lesions–does it increase the healing rate? Eur. J. Pediatr. Surg. 20, 24–28.
Langergren, S.Y.D., 1898. Zur theorie der Sogenannten adsorption gelöster stoffe. K. - Sven. Vetenskapsakademiens Handl. 24, 1–39.
Li, H., Yu, H., Zhai, J., Sun, L., Yang, H., Xie, S., 2015. Self-assembled 3D cobalt phosphate octahydrate architecture for supercapacitor electrodes. Mater. Lett. 152, 25–28.
Li, J., Zhang, L., Yang, P., Cheng, X., 2018. Morphological evolution of Co phosphate and its electrochemical and photocatalytic performance. CrystEngComm 20, 6982–6988.
Liu, X., Huang, Y., Duan, S., Wang, Y., Li, J., Chen, Y., Hayat, T., Wang, X., 2016. Graphene oxides with different oxidation degrees for Co(II) ion pollution management. Chem. Eng. J. 302, 763–772.
Lu, B.Q., Willhammar, T., Sun, B.B., Hedin, N., Gale, J.D., Gebauer, D., 2020. Introducing the crystalline phase of dicalcium phosphate monohydrate. Nat. Commun. 11, 1546.
Manciu, M., Ruckenstein, E., 2001. Role of hydration force in the stability of colloids at high ionic strengths. Langmuir 17, 7061–7070.
Marx, D., Chandra, A., Tuckerman, M.E., 2010. Aqueous basic solutions: hydroxide solvation, structural diffusion, and comparison to the hydrated proton. Chem. Rev. 110, 2174–2216.
Mohd Shafie, E.R., Ahmad, Z.A., Ahmad, N., 2017. Study on conversion time of brushite to monetite via hydrothermal method. Mater. Sci. Forum 888, 319–323.
Mourabet, M., El Boujaady, H., El Rhilassi, A., Ramdane, H., Bennani-Ziatni, M., El Hamri, R., Taitai, A., 2011. Defluoridation of water using Brushite: equilibrium, kinetic and thermodynamic studies. Desalination 278, 1–9.
Nightingale Jr., E.R., 1959. Phenomological theory of ion solvation. Effective radii of hydrated ions. J. Phys. Chem. 63, 1381–1387.
Pan, X., Wang, J., Zhang, D., 2009. Sorption of cobalt to bone char: kinetics, competitive sorption and mechanism. Desalination 249, 609–614.
Pearson, R.G., 1988. Absolute electronegativity and hardness: application to inorganic chemistry. Inorg. Chem. 27, 734–740.
Plecas, I., Pavlovic, R., Pavlovic, S., 2002. Immobilization of Cs-137, Co-60, Mn-54 and Sr-85 in cement-waste composition. In: International Meeting: Clays in Natural and Engineered Barriers for Radioactive Waste Confinement, Reims, France, pp. 351–352.
Qin, L., Zhang, W., Lu, J., Stack, A.G., Wang, L., 2013. Direct imaging of nanoscale dissolution of dicalcium phosphate dihydrate by an organic ligand: concentration matters. Environ. Sci. Technol. 47, 13365–13374.
Rocha, D.N.d., Silva, M.H.P.d., Campos, J.B.d., Marçal, R.L.S.B., Mijares, D.Q., Coelho, P. G., Cruz, L.R., 2018. Kinetics of conversion of brushite coatings to hydroxyapatite in alkaline solution. Journal of Materials Research and Technology 7, 479–486.
Ruiz-Agudo, E., Urosevic, M., Putnis, C.V., Rodríguez-Navarro, C., Cardell, C., Putnis, A., 2011. Ion-specific effects on the kinetics of mineral dissolution. Chem. Geol. 281, 364–371.
Schofield, P.F., Knight, K.S., Houwen, J.A.M.v.d., Valsami-Jones, E., 2004. The role of hydrogen bonding in the thermal expansion and dehydration of brushite, di-calcium phosphate dihydrate. Phys. Chem. Miner. 31, 606–624.
Shibi, I.G., Anirudhan, T.S., 2005. Adsorption of Co(II) by a carboxylate-functionalized polyacrylamide grafted lignocellulosics. Chemosphere 58, 1117–1126.
Smiciklas, I., Dimovic, I., Mitric, M., 2006. Removal of Co^{2+} from aqueous solutions by hydroxyapatite. Water Res. 40, 2267–2274.
Srivastava, V., Sharma, Y.C., Sillanpää, M., 2015. Application of nano-magnesso ferrite ($n\text{-}MgFe_2O_4$) for the removal of Co^{2+} ions from synthetic wastewater: kinetic, equilibrium and thermodynamic studies. Appl. Surf. Sci. 338, 42–54.
Sugiyama, S., Fujisawa, M., Koizumi, T., Tanimoto, S., Kawashiro, K., Tomida, T., Hayashi, H., 2003. Immobilization of aqueous heavy metal cations with phosphates and sulfates. Bull. Chem. Soc. Jpn. 76, 2419–2422.
Tamimi, F., Le Nihouannen, D., Eimar, H., Sheikh, Z., Komarova, S., Barralet, J., 2012. The effect of autoclaving on the physical and biological properties of dicalcium phosphate dihydrate bioceramics: brushite vs. monetite. Acta Biomater. 8, 3161–3169.
Tang, R., Orme, C.A., Nancollas, G.H., 2003. A new understanding of demineralization: the dynamics of brushite dissolution. J. Phys. Chem. B 107, 10653–10657.
Tas, A.C., McKittrick, J., 2016. Transformation of Brushite ($CaHPO_4{\cdot}2H_2O$) to Whitlockite ($Ca_9Mg(HPO_4)(PO_4)_6$) or other CaPs in physiologically relevant solutions. J. Am. Ceram. Soc. 99, 1200–1206.
Tsai, S.-C., Juang, K.-W., 2000. Comparison of linear and nonlinear forms of isotherm models for strontium sorption on a sodium bentonite. J. Radioanal. Nucl. Chem. 243, 741–746.
Turner, R.J., Renshaw, J.C., Hamilton, A., 2017. Biogenic hydroxyapatite: a new material for the preservation and restoration of the built environment. ACS Appl. Mater. Interfaces 9, 31401–31410.
Valsami-Jones, E., Ragnarsdottir, K.V., Putnis, A., Bosbach, D., Kemp, A.J., Cressey, G., 1998. The dissolution of apatite in the presence of aqueous metal cations at pH 2-7. Chem. Geol. 151, 215–233.
Vivas, E.L., Lee, S., Cho, K., 2020. Brushite-infused polyacrylonitrile nanofiber adsorbent for strontium removal from water. J. Environ. Manag. 270.
Weber, W.J., Morris, J.C., 1963. Kinetics of adsorption on carbon from solution. J. Sanit. Eng. Div. 89, 31–60.
Xiao, Y., Azaiez, J., Hill, J.M., 2018. Erroneous application of pseudo-second-order adsorption kinetics model: ignored assumptions and spurious correlations. Ind. Eng. Chem. Res. 57, 2705–2709.
Zhai, H., Wang, L., Qin, L., Zhang, W., Putnis, C.V., Putnis, A., 2018. Direct observation of simultaneous immobilization of cadmium and arsenate at the brushite-fluid interface. Environ. Sci. Technol. 52, 3493–3502.